Monthly Notices of the ROYAL ASTRONOMICAL SOCIETY

MNRAS **474,** 2334–2351 (2018) doi:10.1093/mnras/stx2896
Advance Access publication 2017 November 13

High-precision multiwavelength eclipse photometry of the ultra-hot gas giant exoplanet WASP-103 b

L. Delrez,[1,2]★ N. Madhusudhan,[3] M. Lendl,[4,5,6] M. Gillon,[2] D. R. Anderson,[7] M. Neveu-VanMalle,[5] F. Bouchy,[5] A. Burdanov,[2] A. Collier-Cameron,[8] B.-O. Demory,[1,9] C. Hellier,[7] E. Jehin,[2] P. Magain,[2] P. F. L. Maxted,[7] D. Queloz,[1,5] B. Smalley[7] and A. H. M. J. Triaud[3]

[1]*Astrophysics Group, Cavendish Laboratory, J.J. Thomson Avenue, Cambridge CB3 0HE, UK*
[2]*Space sciences, Technologies and Astrophysics Research (STAR) Institute, Université de Liège, allée du 6 Août 17, 4000 Liège, Belgium*
[3]*Institute of Astronomy, University of Cambridge, Cambridge CB3 0HA, UK*
[4]*Space Research Institute, Austrian Academy of Sciences, Schmiedlstr. 6, A-8042 Graz, Austria*
[5]*Observatoire de Genève, Université de Genève, 51 Chemin des Maillettes, CH-1290 Sauverny, Switzerland*
[6]*Max Planck Institute for Astronomy, Königstuhl 17, D-69117 Heidelberg, Germany*
[7]*Astrophysics Group, Keele University, Staffordshire, ST5 5BG, UK*
[8]*SUPA, School of Physics and Astronomy, University of St. Andrews, North Haugh, Fife, KY16 9SS, UK*
[9]*University of Bern, Centre for Space and Habitability, Sidlerstrasse 5, CH-3012, Bern, Switzerland*

Accepted 2017 November 6. Received 2017 November 6; in original form 2017 January 20

ABSTRACT

We present 16 occultation and three transit light curves for the ultra-short period hot Jupiter WASP-103b, in addition to five new radial velocity measurements. We combine these observations with archival data and perform a global analysis of the resulting extensive data set, accounting for the contamination from a nearby star. We detect the thermal emission of the planet in both the z' and K_S bands, the measured occultation depths being 699±110 ppm (6.4σ) and 3567^{+400}_{-350} ppm (10.2σ), respectively. We use these two measurements, together with recently published HST/WFC3 data, to derive joint constraints on the properties of WASP-103b's dayside atmosphere. On one hand, we find that the z' band and WFC3 data are best fit by an isothermal atmosphere at 2900 K or an atmosphere with a low H_2O abundance. On the other hand, we find an unexpected excess in the K_S band measured flux compared to these models, which requires confirmation with additional observations before any interpretation can be given. From our global data analysis, we also derive a broad-band optical transmission spectrum that shows a minimum around 700 nm and increasing values towards both shorter and longer wavelengths. This is in agreement with a previous study based on a large fraction of the archival transit light curves used in our analysis. The unusual profile of this transmission spectrum is poorly matched by theoretical spectra and is not confirmed by more recent observations at higher spectral resolution. Additional data, in both emission and transmission, are required to better constrain the atmospheric properties of WASP-103b.

Key words: techniques: photometric – techniques: radial velocities – planets and satellites: atmospheres – stars: individual: WASP-103 – planetary systems.

1 INTRODUCTION

Transiting extrasolar planets are key objects for the understanding of worlds beyond our Solar system, as they provide a wealth of information about their systems. Thanks to their special orbital configuration, we can not only measure their radius, true mass (either by radial velocity measurements or via transit timing variations in multiplanet systems), and orbital parameters, but we can also study their atmosphere and thus gain a complete picture of their chemical and physical properties (e.g. Deming & Seager 2009; Winn 2010; Burrows 2014; Madhusudhan et al. 2016). These atmospheric studies are conducted using mainly the transmission and emission (spectro)photometry techniques. During a transit,

★ E-mail: lcd44@cam.ac.uk

some of the starlight passes through the planetary atmosphere and, depending on the atmospheric extent, temperature, and composition, wavelength-dependent variations are seen in the amount of absorbed flux. Thus, from multiwavelength transit light curves, a transmission spectrum of the upper atmosphere at the day–night terminator region can be obtained (e.g. Seager & Sasselov 2000; Charbonneau et al. 2002). At the opposite conjunction, when the planet passes behind the star during a secondary eclipse (occultation), one can measure the flux drop caused by the elimination of the flux component originating from the dayside of the planet (e.g. Charbonneau et al. 2005; Deming et al. 2005). Using this technique at different wavelengths allows us to probe the emission spectrum of the planet's dayside, from which insights on its atmospheric composition and vertical pressure-temperature ($P - T$) profile can be gained.

A broad diversity of transmission spectra has been found across the population of close-in transiting gas giant exoplanets (see e.g. Sing et al. 2016; Fu et al. 2017; Tsiaras et al. 2017). Some planets have sufficiently clear atmospheres to allow detections of atomic and molecular species, in particular Na (e.g. Nikolov et al. 2014), K (e.g. Sing et al. 2011) and H_2O (e.g. Deming et al. 2013), while others appear to contain high-altitude clouds or hazes that completely mute the spectral features of the atmospheric components (see e.g. Gibson et al. 2013; Line et al. 2013; Lendl et al. 2016). Even when detected, atmospheric spectral signatures are often less pronounced than predicted by theoretical models of clear atmospheres with solar abundances (e.g. Deming et al. 2013; Madhusudhan et al. 2014), suggesting that an extra opacity source is still present, at some level, in otherwise predominantly cloud-free atmospheres. This picture is supported by evidences for high-altitude atmospheric hazes reported for several hot Jupiters (see e.g. Nikolov et al. 2015; Sing et al. 2015, 2016), based on their Rayleigh or Mie scattering signature in the planets' transmission spectra.

On the emission side, most observations gathered so far seem to indicate atmospheric vertical pressure-temperature profiles without significant thermal inversions. Temperature inversions were predicted by early theoretical studies of highly irradiated giant planets, that suggested two classes of hot Jupiters based on their degree of irradiation (e.g. Hubeny, Burrows & Sudarsky 2003; Fortney et al. 2008); the hotter class was predicted to host thermal inversions in their atmospheres due to strong absorption of incident UV/visible irradiation at high altitude by high-temperature absorbers, such as gaseous TiO and VO (commonly found in low-mass stars and brown dwarfs), while cooler atmospheres were expected to be devoid of thermal inversions due to the condensation of these absorbing compounds. Thermal inversions have been previously claimed for several hot Jupiters based on *Spitzer* observations (e.g. Knutson et al. 2008; Machalek et al. 2008; Knutson et al. 2009), but these detections have been seriously called into question since then (e.g. Diamond-Lowe et al. 2014; Hansen, Schwartz & Cowan 2014; Schwarz et al. 2015). It has been suggested that TiO and VO may not remain suspended in the upper atmospheres of hot Jupiters due to cold-trapping, that would occur either deeper in the dayside atmosphere or on the cooler nightside, and would cause their condensation and downward drag by gravitational settling (e.g. Spiegel, Silverio & Burrows 2009). Inversion-causing compounds may also be photodissociated by high chromospheric emission from the host star, so that the formation of inversions may be affected by stellar activity (e.g. Knutson, Howard & Isaacson 2010). Another important factor is the atmospheric chemistry; for example, the atmospheric carbon-to-oxygen ratio (C/O) can control the abundance of TiO/VO, with a C/O $\geq$ 1 causing substantial depletion of TiO/VO, most available oxygen being taken up by CO molecules in this case, thus leaving no oxygen for gaseous TiO/VO (Madhusudhan 2012). Alternatively, the apparently isothermal emission spectra observed for many hot Jupiters (e.g. Hansen et al. 2014) may result from the presence of high-altitude cloud decks in their dayside atmospheres that could prevent some thermal inversions from being detected (e.g. Sing et al. 2013). Nevertheless, hottest planets are still the best candidates to look for thermal inversions. Indeed, the planets showing the strongest evidence to date for temperature inversions are WASP-33 b (Haynes et al. 2015; Nugroho et al. 2017) and WASP-121 b (Evans et al. 2017), which are among the most highly irradiated hot Jupiters currently known. In this work, we study the atmospheric properties of another ultra-hot gas giant, WASP-103 b (Gillon et al. 2014, hereafter G14).

This extreme hot Jupiter, discovered by the WASP Collaboration (Pollacco et al. 2006; Collier Cameron et al. 2007; Hellier et al. 2011), has a mass of $\sim$1.5 $M_{\rm Jup}$, an inflated radius of $\sim$1.6 $R_{\rm Jup}$, and is in an ultra-short-period orbit ($\sim$22.2 h) around a relatively bright ($V = 12.1$, $K = 10.8$) F8V star (G14). With an incident stellar flux of $\sim 9.1 \times 10^9$ erg s^{-1}cm^{-2} ($\sim 9.1 \times 10^6$ W m^{-2}), it is one of the most highly irradiated hot Jupiters known to date. Assuming a null Bond albedo, it is heated to an equilibrium temperature close to 2500 K. These properties make WASP-103 b an exquisite target for atmospheric characterization. Another interesting fact about this planet is that its orbital semimajor axis is also only $\sim$1.16 times larger than its Roche limit, meaning that the planet might be close to tidal disruption. WASP-103 b is thus also a favorable object for studying the atmospheric properties of hot Jupiters in the last stages of their evolution.

Southworth et al. (2015, hereafter S15) published high-precision follow-up transit photometry of WASP-103 b in several broad-band optical filters, which they used to refine the physical and orbital parameters of the system. They also detected a slope in the resulting broad-band transmission spectrum, larger values of the effective planetary radius being obtained at bluer wavelengths, which they found to be too steep to be mainly caused by Rayleigh scattering in the planetary atmosphere. Subsequent to their study, a previously unresolved faint star was found via lucky imaging by Wöllert & Brandner (2015, hereafter W15) at an angular separation of only 0.24 arcsec from WASP-103. This object, which was also recently imaged by Ngo et al. (2016, hereafter N16), is significantly redder than WASP-103 and may be either gravitationally bound or simply aligned along the line of sight. Contamination from this redder star, if not accounted for, is expected to produce a blueward slope in the transmission spectrum of WASP-103 b, the transit signal being more strongly diluted at longer wavelengths than at shorter ones. This led Southworth & Evans (2016, hereafter S16) to publish a reanalysis of the data presented in S15, accounting for the presence of the contaminating star. They found the inclusion of contaminating light from the faint star in their analysis to have no significant effect on the derived system physical properties. They also reported a corrected broad-band transmission spectrum showing, instead of a steep slope, a minimum effective planetary radius around 760 nm and increasing values towards both bluer and redder wavelengths. This 'V-shape is not well reproduced by existing theoretical models of transmission spectra. Very recently, Lendl et al. (2017) reported an optical transmission spectrum of WASP-103 b obtained at medium spectral resolution between 550 and 960 nm using Gemini/GMOS. While they found signs of strong Na and K absorption, they did not observe any evidence for the V-shape pattern reported by S16.

Recently, Cartier et al. (2017, hereafter C17) presented near-infrared occultation spectrophotometry of WASP-103 b obtained using the *Hubble Space Telescope*/Wide Field Camera 3. After cor-

rection for flux contamination from the nearby star, they found the dayside emission spectrum of WASP-103 b to be indistinguishable from isothermal from 1.1 to 1.7 μm. They noted that several atmospheric models, besides an isothermal one, can result in an apparently isothermal emission spectrum across this wavelength range, for example an atmosphere with a thermal inversion layer just above the layer probed by their observations, an atmosphere with a monotonically decreasing temperature-pressure profile and a C/O>1, or an atmosphere harbouring clouds or hazes at high altitude. This highlights the need for additional eclipse observations at other wavelengths to help differentiate between these potential atmospheric scenarios.

To improve the atmospheric characterization of WASP-103 b, we carried out an intense ground-based photometric monitoring of its occultations, with the aim of probing its dayside emission spectrum in the z' (0.9 μm) and K_S (2.1 μm) bands. We complemented the data acquired in the frame of this program with some additional transit photometry and radial velocity (RV) measurements, combined all these new observations with the data previously published in G14 and S15, and performed a global analysis of the resulting extensive data set, taking into account the contamination from the faint star. The Gemini/GMOS transmission and HST/WFC3 emission data were published during the final stages of the preparation of this manuscript, so we did not include them in our global analysis but we discuss these measurements along with our results in the scientific discussion. The paper is organized as follows. The new observations and their reduction are described in Section 2, as well as the archival data used in our global analysis. In Section 3, we present our detailed data analysis and results. We discuss these results in Section 4, before concluding in Section 5.

2 OBSERVATIONS AND DATA REDUCTION

2.1 New data

Between May 2014 and July 2015, we gathered a total of 19 eclipse light curves of WASP-103 b. Sixteen of these light curves were acquired during occultations of the planet and three during transits. This follow-up photometry was obtained using three different instruments: the 0.6m TRAPPIST robotic telescope and the EulerCam CCD camera on the 1.2 m *Euler*-Swiss telescope, both located at ESO La Silla Observatory (Chile), as well as the WIRCam near-infrared imager on the 3.6 m Canada-France-Hawaii Telescope (CFHT) at Mauna Kea Observatory (Hawaii). We complemented this data set with five new RV measurements obtained between 2013 September and 2014 September with the CORALIE spectrograph mounted on the *Euler* telescope. The follow-up light curves are summarized in the upper part of Table 1, while the RVs are presented in Table 2. We describe these new data in the sections below.

2.1.1 TRAPPIST eclipse photometry

We observed one transit and nine occultations of WASP-103 b using the 0.6 m TRAPPIST robotic telescope and its thermoelectrically-cooled 2K×2K CCD (field of view of 22 arcmin ×22 arcmin, plate scale of 0.65 arcsec pixel^{-1}). For details of TRAPPIST, see Gillon et al. (2011a) and Jehin et al. (2011). The transit was observed in a blue-blocking (*BB*) filter that has a transmittance >90 per cent from 500 nm to beyond 1000 nm (effective wavelength = 696.8 nm), with each frame exposed for 8 s. The occultations were acquired through a Sloan-z' filter (effective wavelength = 895.5 nm), with exposure times between 36 s and 55 s. Throughout observations, the telescope was kept in focus and the positions of the stars on the chip were retained on the same few pixels, thanks to a 'software guiding' system that regularly derives an astrometric solution on the images and sends pointing corrections to the mount when needed.

After bias, dark, and flat-field corrections, stellar fluxes were extracted from the images using the IRAF/DAOPHOT[1] aperture photometry software (Stetson 1987). For each observation, a careful selection of both the photometric aperture size and of stable reference stars having a brightness similar to WASP-103 was performed to obtain optimal differential photometry. The resulting light curves are shown in Figs A1 (raw occultation light curves), A2 (detrended occultation light curves; see Section 3.2 for details about the modelling) and A3 (raw transit light curve).

2.1.2 Euler/EulerCam eclipse photometry

Two transit and six occultation light curves of WASP-103 b were obtained with EulerCam, the imager of the 1.2 m *Euler*-Swiss telescope. EulerCam is a nitrogen-cooled 4K×4K CCD camera with a field of view of 15.68arcmin ×15.73arcmin at a plate scale of 0.215arcsec pixel^{-1}. The transits were observed in a Gunn-r' filter (effective wavelength = 664.1 nm) with an exposure time of 80 s. The occultations were acquired through a Gunn-z' filter (effective wavelength = 912.3 nm), with exposure times between 60 and 100 s. A slight defocus was applied to the telescope to optimize the observation efficiency and to minimize pixel-to-pixel effects. This resulted in stellar PSFs with a typical FWHM between 1.1 and 2.5 arcsec. Here too, the positions of the stars on the detector were kept within a box of a few pixels throughout the observations, thanks to the 'Absolute Tracking' system of EulerCam that matches the point sources in each image with a catalogue and adjusts the telescope pointing between exposures when needed. The reduction procedure used to extract the eclipse light curves was similar to that performed on TRAPPIST data. The resulting light curves are shown in Figs A1 (raw occultation light curves), A2 (detrended occultation light curves; see Section 3.2 for details about the modelling) and A3 (raw transit light curves). Further details of the EulerCam instrument and data reduction procedures can be found in Lendl et al. (2012).

2.1.3 CFHT/WIRCam occultation photometry

We observed one occultation of WASP-103 b with the Wide-field InfraRed Camera (WIRCam; Puget et al. 2004) on the 3.6 m Canada-France-Hawaii Telescope. WIRCam consists of four 2K×2K HgCdTe HAWAII-2RG arrays, arranged in a 2×2 mosaic. The instrument has a total field of view of 20.5 arcmin×20.5 arcmin (with gaps of 45 arcsec between adjacent chips) at a scale of 0.3arcsec pixel^{-1}. We used the K_S broad-band filter, which has a bandwidth of 0.325 μm centred at 2.146 μm. The observations took place on 2014 May 20 from 06:50 to 12:40 UT, covering the 2.6 h long predicted occultation (assuming a circular orbit) together with 3.2 h of out-of-eclipse observations. Conditions were photometric,

[1] IRAF is distributed by the National Optical Astronomy Observatory, which is operated by the Association of Universities for Research in Astronomy, Inc., under cooperative agreement with the National Science Foundation.

Table 1. Summary of follow-up photometry obtained for WASP-103. For each light curve, this table shows the night of acquisition (UT), the used instrument, the eclipse type, the filter (*BB*=blue-blocking) and exposure time, the number of data points, the selected baseline function, the standard deviation of the best-fitting residuals (unbinned and binned per intervals of 2 min), and the deduced values for β_w, β_r and $CF = \beta_w \times \beta_r$ (see Section 3.2 for details). For the baseline function, $p(\epsilon^N)$ denotes, respectively, a N-order polynomial function of time ($\epsilon = t$), airmass ($\epsilon = a$), PSF full-width at half-maximum ($\epsilon = f$) or radius for the WIRCam data ($\epsilon = r$), background ($\epsilon = b$), and x and y positions ($\epsilon = xy$). o denotes an offset fixed at the time of the meridian flip.

Date (UT)	Instrument	Eclipse type	Filter	T_{exp} (s)	N_p	Baseline function	σ (per cent)	σ_{120s} (per cent)	β_w	β_r	CF
New data											
2014 May 8–9	TRAPPIST	Occultation	z'	55	338	$p(t^1) + o$	0.25	0.19	1.10	1.08	1.18
2014 May 20–20	WIRCam	Occultation	K_S	5	1083	$p(t^2+r^1+b^1)$	0.32	0.12	1.56	1.00	1.57
2014 June 10–11	EulerCam	Transit	r'	80	140	$p(t^1+b^1)$	0.18	0.18	1.89	1.00	1.89
2014 June 16–17	TRAPPIST	Occultation	z'	50	341	$p(t^1) + o$	0.25	0.18	1.08	1.07	1.16
2014 June 29–30	EulerCam	Occultation	z'	100	130	$p(t^1+f^1)$	0.10	0.10	1.20	1.00	1.20
2014 July 5–6	EulerCam	Transit	r'	80	150	$p(t^1)$	0.09	0.09	1.16	1.49	1.72
2014 July 11–12	EulerCam	Occultation	z'	100	65	$p(t^1+b^1)$	0.09	0.09	1.18	1.10	1.30
2014 July 12–13	TRAPPIST	Occultation	z'	48	281	$p(t^1) + o$	0.26	0.18	1.05	1.91	2.01
2014 July 25–26	TRAPPIST	Occultation	z'	48	308	$p(t^1) + o$	0.23	0.16	1.00	1.10	1.10
2015 Apr. 2–3	TRAPPIST	Transit	*BB*	8	910	$p(a^1) + o$	0.35	0.14	0.87	1.08	0.95
2015 May 17–18	TRAPPIST	Occultation	z'	36	328	$p(t^1) + o$	0.32	0.23	1.28	1.22	1.56
2015 May 30–31	TRAPPIST	Occultation	z'	36	364	$p(a^1) + o$	0.36	0.26	1.32	1.00	1.32
2015 June 11–12	EulerCam	Occultation	z'	100	139	$p(t^2+f^1+b^1)$	0.14	0.14	1.56	2.10	3.27
2015 June 12–13	TRAPPIST	Occultation	z'	40	315	$p(a^1) + o$	0.36	0.26	1.43	1.00	1.43
2015 July 7–8	TRAPPIST	Occultation	z'	46	365	$p(t^1) + o$	0.30	0.22	1.29	1.51	1.94
2015 July 7–8	EulerCam	Occultation	z'	100	126	$p(a^2+f^1+b^1)$	0.11	0.11	1.27	1.42	1.82
2015 July 19–20	TRAPPIST	Occultation	z'	46	327	$p(t^1) + o$	0.35	0.24	1.37	1.17	1.60
2015 July 19–20	EulerCam	Occultation	z'	100	134	$p(t^1+f^1+b^1)$	0.10	0.10	1.13	1.22	1.39
2015 July 20–21	EulerCam	Occultation	z'	60	210	$p(t^1+f^1)$	0.10	0.08	1.10	1.37	1.51
Archival data											
2013 June 15–16	TRAPPIST	Transit	*BB*	7	802	$p(t^1+f^1) + o$	0.32	0.13	0.69	1.48	1.02
2013 June 28–29	EulerCam	Transit	r'	120	103	$p(t^1+f^1+b^2+xy^1)$	0.09	0.09	1.43	1.08	1.54
2013 July 11–12	EulerCam	Transit	r'	80	105	$p(t^1+b^1)$	0.12	0.12	1.59	1.23	1.96
2013 July 23–24	TRAPPIST	Transit	*BB*	9	941	$p(t^2) + o$	0.48	0.19	1.23	1.22	1.50
2013 Aug. 4–5	TRAPPIST	Transit	*BB*	10	935	$p(t^2) + o$	0.29	0.13	0.80	1.51	1.21
2014 Apr. 19–20	DFOSC	Transit	*R*	100–105	134	$p(t^1)$	0.07	0.07	1.05	2.53	2.65
2014 May 1–2	DFOSC	Transit	*I*	110–130	113	$p(t^1)$	0.08	0.08	1.06	1.14	1.21
2014 June 8–9	DFOSC	Transit	*R*	100–130	130	$p(t^1)$	0.10	0.10	1.03	1.41	1.45
2014 June 22–23	DFOSC	Transit	*R*	50–120	195	$p(t^1)$	0.13	0.13	1.05	2.62	2.75
2014 June 23–24	DFOSC	Transit	*R*	100	112	$p(t^1)$	0.06	0.06	1.01	1.44	1.45
2014 July 5–6	DFOSC	Transit	*R*	100	118	$p(t^1)$	0.06	0.06	1.01	1.81	1.83
2014 July 5–6	GROND	Transit	g'	100–120	122	$p(t^2)$	0.12	0.12	1.03	1.44	1.49
2014 July 5–6	GROND	Transit	r'	100–120	125	$p(t^2)$	0.07	0.07	1.01	2.20	2.22
2014 July 5–6	GROND	Transit	i'	100–120	119	$p(t^2)$	0.08	0.08	1.04	1.42	1.48
2014 July 5–6	GROND	Transit	z'	100–120	121	$p(t^2)$	0.11	0.11	1.03	2.49	2.58
2014 July 17–18	DFOSC	Transit	*R*	90–110	139	$p(t^1)$	0.07	0.07	1.00	1.21	1.22
2014 July 18–19	DFOSC	Transit	*R*	60–110	181	$p(t^2)$	0.06	0.05	1.02	1.19	1.21
2014 July 18–19	GROND	Transit	g'	98–108	126	$p(t^2)$	0.08	0.08	1.02	1.44	1.48
2014 July 18–19	GROND	Transit	r'	98–108	143	$p(t^2)$	0.06	0.06	1.04	1.64	1.70
2014 July 18–19	GROND	Transit	i'	98–108	142	$p(t^2)$	0.09	0.09	1.05	1.66	1.74
2014 July 18–19	GROND	Transit	z'	98–108	144	$p(t^2)$	0.09	0.09	1.01	1.13	1.14
2014 Aug. 12–13	CASLEO	Transit	*R*	90–120	129	$p(t^2)$	0.15	0.15	1.04	1.51	1.58

with a median seeing of 0.6 arcsec, and airmass decreased from 2.4 to 1.09 during the run. The data were gathered in staring mode (Devost et al. 2010), with the target and reference stars observed continuously for several hours on the same pixels without any dithering. This mode has been used by other authors for similar observations with WIRCam (see e.g. Wang et al. 2013; Croll et al. 2015) and has proven to yield an optimal photometric precision. The pointing was carefully selected to ensure that the target and reference stars did not fall near bad pixels, as well as to maximize the number of suitable reference stars located on the same WIRCam chip as WASP-103 (see below). The scientific sequence consisted of 1092 exposures, each 5 s and read out with correlated double sampling[2] (CDS). A defocus of 2 mm was applied to the telescope, in order to reduce the impact of imperfect flat-fielding, inter- and intrapixel variations on the photometry, as well as to keep the counts of the target and reference stars in the regime where detector non-linearity

[2] A CDS image is constructed by subtracting a first read of the array, done immediately after reset, from a second read of the array, performed at the end of the exposure.

Table 2. New CORALIE RVs for WASP-103. The last two columns give the cross-correlation function FWHM and bisector span values, respectively.

BJD −2 450 000	RV (km s^{-1})	σ_{RV} (km s^{-1})	FWHM (km s^{-1})	BS (km s^{-1})
6537.506 214	−42.194 67	0.129 30	15.478 57	0.048 12
6837.661 259	−41.954 97	0.057 63	14.906 43	0.074 58
6852.650 727	−41.782 95	0.062 56	14.925 42	0.265 43
6880.562 742	−41.579 79	0.070 13	15.074 07	0.454 40
6920.487 957	−41.866 93	0.098 04	14.646 20	−0.401 81

is minimized (linearity to within 1 per cent below ∼10 kADU)[3]. This resulted in a ring-shaped PSF with a radius of ∼4.5 arcsec (∼15 pixels). A short set of dithered (10 offset positions) in-focus images was taken before and after the scientific sequence in order to construct a sky flat (see below).

The data were reduced independently of the traditional WIRCam ʻIʻiwi pipeline[4], following the prescription of Croll et al. (2015) for the reduction of WIRCam staring mode data. We refer the reader to that paper for a detailed description of the reduction procedure and give here an outline of the main steps. The frames from each detector were reduced separately. In each image, the pixels with CDS values above 36 kADU were flagged as saturated. The data were corrected for the small non-linearity present below 10 kADU, following the iterative approach of Vacca, Cushing & Rayner (2004) for applying a non-linearity correction to CDS images. Each frame was dark subtracted and divided by a sky flat, which was created by taking the median stack of the dithered images acquired before and after the scientific sequence. A bad pixel map was constructed from this sky flat, where pixels flagged as bad were those that deviate by more than 2 per cent from the median of the array. Finally, in each image, bad and saturated pixels had their value replaced by the median value of the adjacent pixels (provided that they were not themselves bad or saturated).

Aperture photometry was performed for the target and reference stars using IRAF/DAOPHOT. Apertures were centred using intensity-weighted centroids. We tested a set of constant apertures, as well as apertures that varied from image to image as a function of the mean radius of the ring-shaped stellar PSFs. The best result was obtained with a variable aperture of 1.1 times the mean radius. Using a variable photometric aperture, rather than a fixed one, allowed us to account for the varying atmospheric conditions, as well as to find for each individual image a balance between choosing a small aperture to minimize the sky noise and a large aperture to encompass all the stellar light. For other examples of exoplanet near-infrared photometry extracted using a variable aperture size, see e.g. Lendl et al. (2013) or Zhou et al. (2014). The sky annulus was kept constant for all images, with an inner radius of 30 pixels and an outer radius of 50 pixels. Differential photometry of WASP-103 was finally obtained. We tested all possible combinations of stable reference stars having a brightness similar to the target. We found the best photometry using eight reference stars located on the same WIRCam detector as WASP-103. The resulting light curve is shown in Fig. 1 .

[3] www.cfht.hawaii.edu/Instruments/Imaging/WIRCam/WIRCamNonlinearity.html

[4] http://www.cfht.hawaii.edu/Instruments/Imaging/WIRCam/IiwiVersion2Doc.html

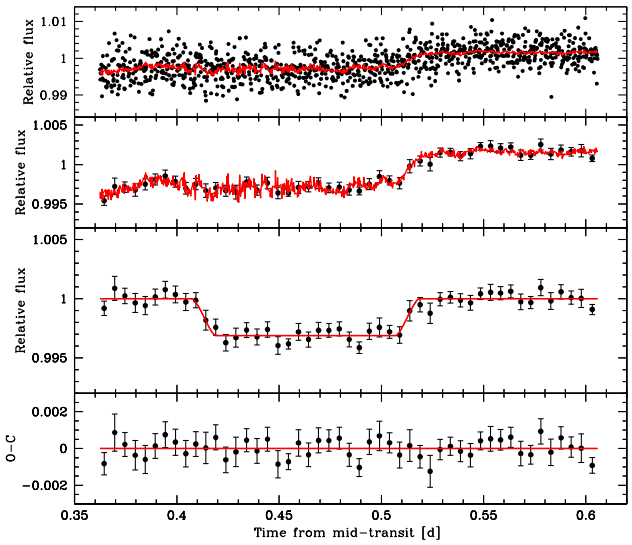

Figure 1. Occultation photometry obtained with CFHT/WIRCam in the K_S band. Top panel: the raw, unbinned light curve, together with the best-fitting full (photometric baseline × occultation in the K_S band) model (overplotted in red; see Section 3.2 for details about the modelling). Second panel: same as the top panel except that the data are binned in 7.2 min bins. Third panel: binned light curve divided by the best-fitting photometric baseline model. The best-fitting occultation model in the K_S band is overplotted in red. Bottom panel: best-fitting residuals. The RMS of the residuals is 524 ppm (7.2 min bins). General note: the data and models are not corrected for the dilution by the nearby star here.

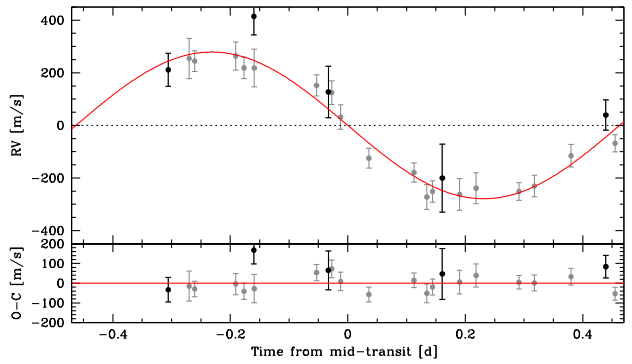

Figure 2. Top: Euler/CORALIE RV measurements period-folded on the best-fitting transit ephemeris from our global MCMC analysis (see Section 3.2), with the best-fitting Keplerian model overplotted in red. The data published in G14 are plotted in grey, while our new measurements are plotted in black. *Bottom:* corresponding residuals.

2.1.4 *Euler/CORALIE radial velocities*

Five new spectroscopic measurements of WASP-103 were gathered with the CORALIE spectrograph mounted on the *Euler* telescope (Queloz et al. 2000). The spectra, all obtained with an exposure time of 30 min, were processed with the CORALIE standard data reduction pipeline (Baranne et al. 1996). RVs were then computed from the spectra by weighted cross-correlation (Pepe et al. 2002), using a numerical G2-spectral template that provides optimal precisions for late-F to early-K dwarfs. These RVs are presented in Table 2 and shown in Fig. 2. The cross-correlation function (CCF) FWHM and bisector span (BS, Queloz et al. 2001) values are also given in Table 2.

Table 3. Individual apparent magnitudes of WASP-103 and the nearby star in the J, H and K_S bands.

Filter	WASP-103	Contaminant
J	11.210 ± 0.029	13.637 ± 0.053
H	10.993 ± 0.032	13.209 ± 0.039
K_S	10.932 ± 0.023	12.897 ± 0.037

2.2 Archival data

We also included in our global analysis the data previously published in G14 and S15:

(i) three TRAPPIST transit light curves (blue-blocking filter);
(ii) two Euler/EulerCam transit light curves (Gunn-r' filter);
(iii) eight transit light curves gathered with the DFOSC (Danish Faint Object Spectrograph and Camera) instrument on the 1.54 m Danish telescope located at ESO La Silla Observatory (Bessel R and I filters);
(iv) eight transit light curves obtained using the GROND (Gamma-Ray Burst Optical/Near-Infrared Detector) instrument on the 2.2 m MPG/ESO telescope (Sloan-g', -r', -i' and -z' filters);
(v) one transit light curve acquired with the 2.15 m telescope located at the CASLEO (Complejo Astronomico El Leoncito) Observatory (Johnson-Cousins R filter);
(vi) 18 CORALIE RVs.

We refer the reader to G14 and S15 for more details about these data. The archival light curves are summarized in the lower part of Table 1 and shown in Figs A3 (TRAPPIST and Euler/EulerCam), A4 (Danish/DFOSC) and A5 (2.2m/GROND and CASLEO/2.15m), while the RVs are shown in Fig. 2.

3 DATA ANALYSIS

3.1 Contamination from the nearby star

W15 reported the detection of a stellar object located 0.242±0.016 arcsec from WASP-103, fainter by $\Delta i' = 3.11 \pm 0.46$ and $\Delta z' = 2.59 \pm 0.35$. N16 presented further observations of this nearby star in the near-infrared and found magnitude differences with WASP-103 of $\Delta J = 2.427 \pm 0.030$, $\Delta H = 2.2165 \pm 0.0098$ and $\Delta K_S = 1.965 \pm 0.019$. The astrometric measurements from these two studies are inconclusive as to whether this star is gravitationally bound to the planetary system or not. Due to the very small angular separation of WASP-103 and the nearby object, both stars are contained in all photometric apertures used to extract the eclipse light curves that we included in our global analysis (new and archival data). Although a detailed characterization of the nearby star is beyond the scope of this work, we must estimate the dilution correction factor $(F_{W103} + F_{cont})/F_{W103} = 1 + F_{cont}/F_{W103}$ (where F_{cont}/F_{W103} is the contaminant-to-target flux ratio) for each of the observed passbands, in order to account for this contamination in our data analysis.

To this end, we first derived the individual apparent magnitudes of WASP-103 and the nearby star in the J, H and K_S bands based on their combined 2MASS magnitudes (Skrutskie et al. 2006) and the magnitude differences reported by N16 in these bands. The resulting apparent magnitudes are given in Table 3. While the $J - H$, $H - K_S$ and $J - K_S$ colour indices of WASP-103 agree well with a F8V star, the colours of the nearby star suggest a spectral type comprised between K1 and M4 if it is on the main sequence (Straižys & Lazauskaitė 2009). We computed the flux ratios F_{cont}/F_{W103} in the passbands of interest assuming each of these two spectral types for the contaminant. We used for this purpose PHOENIX model spectra (Husser et al. 2013) of WASP-103 and the nearby star that we integrated over the passbands of interest. The flux ratio in a given passband can be expressed as:

$$\frac{F_{cont}}{F_{W103}} = f^2 \frac{M_{cont}}{M_{W103}}, \quad (1)$$

where M_{W103} and M_{cont} are the band-integrated model fluxes of WASP-103 and the contaminant, respectively, and f is a geometric factor defined as:

$$f = \frac{R_{cont}}{R_{W103}} \frac{d_{W103}}{d_{cont}} \quad (2)$$

with R_{W103} (resp. R_{cont}) and d_{W103} (resp. d_{cont}) denoting, respectively, the radius and the distance of WASP-103 (resp. the contaminant). For WASP-103, we used a model spectrum interpolated to the effective temperature T_{eff}, surface gravity $\log g_\star$, and metallicity [Fe/H] reported in G14. For the nearby star, two different model spectra, of typical K1V (T_{eff}=5100 K, $\log g_\star$=4.5, [Fe/H]=0.0) and M4V (T_{eff}=3200 K, $\log g_\star$=5.0, [Fe/H]=0.0) stars, were used. In each of these two cases, we calculated first the wavelength-independent factor f by comparing the ratio of the model fluxes M_{cont}/M_{W103} integrated over the J band with the flux ratio F_{cont}/F_{W103} measured in this band by N16. The flux ratios in the passbands of interest were then computed using Equation (1). The final value for the flux ratio in each passband was taken as the average of the two values obtained using the K1V and M4V model spectra for the contaminating star, with an error bar large enough to encompass both values. The resulting flux ratios are given in Table 4. The values derived in the i' and z' bands are consistent with the measurements from W15 in these two bands (0.0622 ± 0.0250 and 0.0969 ± 0.0302, respectively), but more precise (in the z' band). In the K_S band, we obtained a flux ratio of 0.1496 ± 0.0178, consistent with the value of 0.1637 ± 0.0029 measured by N16, but significantly less precise. For this passband, we thus used the measurement from N16.

Table 4. Contaminant-to-target flux ratios in the observed passbands.

Filter	F_{cont}/F_{W103}
g'	0.0275 ± 0.0243
r'	0.0419 ± 0.0322
R	0.0447 ± 0.0318
BB	0.0552 ± 0.0255
i'	0.0586 ± 0.0250
I	0.0633 ± 0.0236
z'	0.0800 ± 0.0145
K_S	0.1637 ± 0.0029

In their reanalysis, S16 also estimated the contamination from the nearby star in the passbands observed in S15, using the near-infrared magnitude differences reported by N16. They obtained values in good agreement with ours, albeit with much smaller error bars (see the last column of their table 1). This is due to the fact that they only used the ΔJ and ΔK_S magnitude differences, thus discarding the H-band measurement, which results in a smaller uncertainty on the spectral type of the contaminating star. As we see no reason to discard any of the three measurements, we chose to adopt the safer procedure outlined above, giving equal weight to the three colour indices.

3.2 Global data analysis

To obtain the strongest constraints on the system parameters, we performed a global Bayesian analysis of the whole data set (41 eclipse light curves and 23 RVs). We used for this purpose the most recent version of the adaptive Markov Chain Monte Carlo (MCMC) code described in Gillon et al. (2012, and references therein), that derives the posterior probability distribution functions of the global model parameters, basing on stochastic simulations. Each UT time of mid-exposure was converted to the BJD_{TDB} timescale (Eastman, Siverd & Gaudi 2010). To model the photometry, we used the eclipse model of Mandel & Agol (2002) multiplied by a different baseline model for each light curve (see below), while the RVs were modelled using a Keplerian orbit (e.g. Murray & Correia 2010) combined to a systemic velocity. A quadratic limb-darkening law was assumed for the transits.

The photometric baseline models, different for each light curve, allowed to account for photometric variations not related to the eclipses but rather to external astrophysical, instrumental, or environmental effects. They consisted of different polynomials with respect to, e.g. time, airmass, PSF full-width at half-maximum, background, stellar position on the detector, or any combination of these parameters. For each light curve, the optimal baseline function (see Table 1) was selected by way of minimizing the Bayesian Information Criterion (BIC; Schwarz 1978). For the TRAPPIST light curves, a normalization offset was also part of the baseline model to represent the effect of the meridian flip; that is, the 180° rotation that the German equatorial mount telescope has to undergo when the meridian is reached. This movement results in different positions of the stellar images on the detector before and after the flip, and the normalization offset allows to account for a possible consecutive jump in the differential photometry at the time of the flip.

The jump parameters in our MCMC analysis (i.e. the parameters that are randomly perturbed at each step of the MCMC) were:

(i) the transit depth in the R-band $\mathrm{d}F_R = (R_{\mathrm{p},R}/R_\star)^2$, where $R_{\mathrm{p},R}$ is the planetary radius in the R-band and $R_\star$ is the stellar radius;
(ii) the transit depth differences in the other wavelength bands $\mathrm{dd}F_j = \mathrm{d}F_j - \mathrm{d}F_R$ (where $j = g', r', BB, i', I, z'$);
(iii) the occultation depths in the z' and K_S bands, noted $\mathrm{d}F_{\mathrm{occ},z'}$ and $\mathrm{d}F_{\mathrm{occ},K_S}$, respectively;
(iv) the transit impact parameter in the case of a circular orbit $b' = a\cos i_\mathrm{p}/R_\star$, where a is the orbital semi-major axis and i_p is the orbital inclination;
(v) the transit width (from first to fourth contact) W;
(vi) the time of mid-transit T_0;
(vii) the orbital period P;
(viii) the stellar effective temperature T_eff and metallicity [Fe/H];
(ix) the parameter $K_2 = K\sqrt{1-e^2}\ P^{1/3}$, where K is the RV orbital semi-amplitude and e is the orbital eccentricity;
(x) the two parameters $\sqrt{e}\cos\omega$ and $\sqrt{e}\sin\omega$, where ω is the argument of the periastron;
(xi) the linear combinations of the quadratic limb-darkening coefficients ($u_{1,j}$, $u_{2,j}$) in each wavelength band, $c_{1,j} = 2u_{1,j} + u_{2,j}$ and $c_{2,j} = u_{1,j} - 2u_{2,j}$ (where $j = g', r', R, BB, i', I, z'$).

The baseline model parameters were not jump parameters; they were determined by linear least-squares minimization from the residuals at each step of the MCMC, thanks to their linear nature in the baseline functions. For this purpose, a Singular Value Decomposition (SVD) method was used (Press et al. 1992). This approach allows us to increase significantly the efficiency of the MCMC implementation by reducing the number of jump parameters and thus the dimension of the space to probe.

Table 5. Prior probability distribution functions assumed in our MCMC analysis. $\mathcal{N}(\mu, \sigma^2)$ represents a normal distribution with an expectation μ and a variance σ^2.

Parameter	Prior
T_eff	$\mathcal{N}(6110, 160^2)$ K
[Fe/H]	$\mathcal{N}(0.06, 0.13^2)$ dex
$u_{1,g'}$	$\mathcal{N}(0.502, 0.032^2)$
$u_{2,g'}$	$\mathcal{N}(0.253, 0.020^2)$
$u_{1,r'}$	$\mathcal{N}(0.337, 0.024^2)$
$u_{2,r'}$	$\mathcal{N}(0.305, 0.010^2)$
$u_{1,R}$	$\mathcal{N}(0.316, 0.023^2)$
$u_{2,R}$	$\mathcal{N}(0.304, 0.010^2)$
$u_{1,BB}$	$\mathcal{N}(0.316, 0.046^2)$
$u_{2,BB}$	$\mathcal{N}(0.304, 0.020^2)$
$u_{1,i'}$	$\mathcal{N}(0.260, 0.020^2)$
$u_{2,i'}$	$\mathcal{N}(0.298, 0.008^2)$
$u_{1,I}$	$\mathcal{N}(0.242, 0.020^2)$
$u_{2,I}$	$\mathcal{N}(0.296, 0.008^2)$
$u_{1,z'}$	$\mathcal{N}(0.207, 0.018^2)$
$u_{2,z'}$	$\mathcal{N}(0.290, 0.007^2)$

Normal prior probability distribution functions were assumed for T_eff, [Fe/H], $u_{1,j}$, and $u_{2,j}$. For T_eff and [Fe/H], the priors were based on the values reported in G14, with expectations and standard deviations corresponding to the quoted measurements and errors, respectively. As for the normal priors imposed on $u_{1,j}$ and $u_{2,j}$, their parameters were interpolated from the theoretical tables of Claret & Bloemen (2011). All these normal prior distributions are presented in Table 5. Uniform prior distributions were assumed for the other jump parameters. At each MCMC step, a value for $F_\mathrm{cont}/F_\mathrm{W103}$ for each wavelength band was drawn from the normal distribution having as expectation and standard deviation the value and error given in Table 4 for this band, respectively. The dilution correction factor for each band was computed as $1+F_\mathrm{cont}/F_\mathrm{W103}$.

The physical parameters of the system were deduced from the jump parameters at each step of the MCMC, so that their posterior probability distribution functions could also be constructed. At each MCMC step, a value for the stellar mean density $\rho_\star$ was first derived from Kepler's third law and the jump parameters $\mathrm{d}F_R$, b', W, P, $\sqrt{e}\cos\omega$ and $\sqrt{e}\sin\omega$ (see e.g. Seager & Mallén-Ornelas 2003; Winn 2010). This $\rho_\star$ and values for T_eff and [Fe/H] drawn from their normal prior distributions were used to determine a value for the stellar mass $M_\star$ through an empirical law $M_\star(\rho_\star, T_\mathrm{eff}, [\mathrm{Fe/H}])$ (Enoch et al. 2010; Gillon et al. 2011b) that is calibrated using the set of well-constrained detached eclipsing binary (EB) systems presented by Southworth (2011). Here, we chose to reduce this set to the 116 stars with a mass between 0.7 and 1.7 $M_\odot$, with the goal of this selection being to benefit from our preliminary knowledge of the mass of WASP-103 (S15 give $M_\star = 1.204 \pm 0.089\ M_\odot$) to improve the determination of the system parameters. In order to propagate correctly the error on the empirical law, the parameters of the selected subset of calibration stars were normally perturbed within their observational error bars and the coefficients of the law were redetermined at each MCMC step. We furthermore took into account the inability of the empirical law to perfectly reproduce the distribution of the stellar masses by determining at each step of the MCMC the quadratic difference between the RMS of the residuals of the modelling of the EB masses by the empirical law and the mean mass error for the EB sample. At each MCMC step,

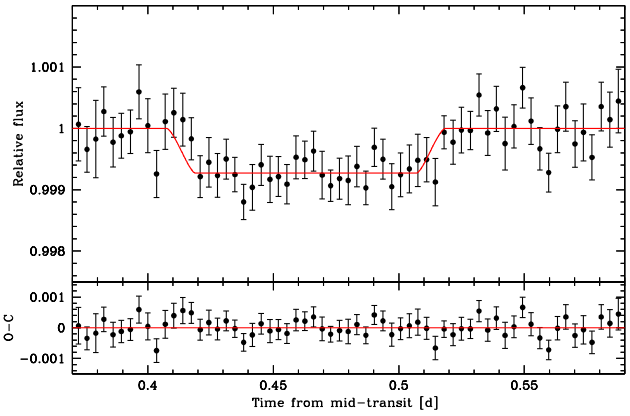

Figure 3. Top: combined occultation photometry obtained in the z' band with TRAPPIST and Euler/EulerCam. The data are period-folded on the best-fitting transit ephemeris from our global MCMC analysis (see Section 3.2), corrected for the photometric baseline, and binned in 5 min bins (for visual convenience). The best-fitting occultation model in the z' band is overplotted in red. The data and model are not corrected for the dilution by the nearby star here. *Bottom:* corresponding residuals. The RMS of the residuals in the shown interval is 305 ppm (5 min bins).

a new value for $M_\star$ was drawn from a normal distribution having as expectation and standard deviation the mass originally determined by the empirical law and the quadratic difference mentioned above, respectively. The stellar radius $R_\star$ was derived from $M_\star$ and $\rho_\star$, and the other physical parameters of the system were then deduced from the jump parameters and stellar mass and radius.

Although the photometric errors were computed considering scintillation, sky, dark, readout and photon noises, they are known to be often moderately underestimated. A preliminary MCMC analysis, consisting of one chain of 50 000 steps, was performed to determine the correction factors CF to be applied to the error bars of each photometric time series, as described in Gillon et al. (2012). For each light curve, CF is the product of two contributions, β_w and β_r. On one side, β_w represents the under- or overestimation of the white noise of each measurement. It is computed as the ratio between the standard deviation of the residuals and the mean photometric error. On the other side, β_r allows us to account for possible correlated noise present in the light curve. It is obtained by comparing the standard deviations of the binned and unbinned residuals for different binning intervals ranging from 5 to 120 min, with the largest value being kept as β_r. The values deduced for β_w, β_r, and $CF = \beta_w \times \beta_r$ for each light curve are given in Table 1. Similarly, this preliminary analysis allowed us to assess the need to rescale the RV error bars, but it was unnecessary here (the best-fitting RV model already gives a reduced $\chi^2 = 1.0$).

With the corrected photometric error bars, two analyses were then performed: one assuming a circular orbit ($e = 0$) and one with a free eccentricity. Each analysis consisted of three chains of 100 000 steps, whose convergence was checked using the statistical test of Gelman & Rubin (1992). The first 20 per cent of each chain was considered as its burn-in phase and discarded. A model comparison based on the Bayes factor, as estimated from the BIC, strongly favoured the circular model (Bayes factor of 4915 in its favour) over the eccentric one. We thus adopted the circular orbit as our nominal solution. The corresponding derived system parameters and 1σ error bars are presented in Table 6. The best-fitting eclipse models are shown in Figs 1 (third panel, occultation model in the K_S band), 3 (occultation model in the z' band) and 4 (transit models in each of the observed passbands), while the best-fitting RV model is displayed in Fig. 2.

4 DISCUSSION

4.1 System physical parameters and correction for asphericity

As expected, we find a slightly larger radius ($1.623^{+0.051}_{-0.053}$ $R_{\rm Jup}$) and a slightly lower mean density ($0.353^{+0.028}_{-0.024}$ $\rho_{\rm Jup}$) for the planet than those reported by G14 ($1.528^{+0.073}_{-0.047}$ $R_{\rm Jup}$, $0.415^{+0.046}_{-0.053}$ $\rho_{\rm Jup}$) and S15 (1.554 ± 0.044 $R_{\rm Jup}$, 0.367 ± 0.027 $\rho_{\rm Jup}$), who did not take into account the contamination from the nearby star, unknown at that time. Our values for these two parameters agree well with those found by S16 ($1.596^{+0.044}_{-0.054}$ $R_{\rm Jup}$, 0.339 ± 0.023 $\rho_{\rm Jup}$). The other physical parameters of the system are in very good agreement with those reported by G14, S15, and S16.

With an orbital semi-major axis only ~1.12 times larger than its Roche limit, WASP-103 b is expected to be significantly deformed by tides (e.g. Budaj 2011). We calculated values for the planetary radius and mean density corrected for asphericity using the same method as S15 (also applied to the case of WASP-121 b by Delrez et al. 2016). In brief, we used the Roche model of Budaj (2011) to compute the Roche shape of the planet which would have the same cross-section during transit as the one we inferred from our observations assuming a spherical planet (eclipse model of Mandel & Agol 2002; see Section 3.2). The main inputs of the model were the orbital semi-major axis ($a = 4.26^{+0.12}_{-0.13}$ $R_\odot$), the star-to-planet mass ratio ($M_\star/M_{\rm p} = 840 \pm 137$) and the planetary radius obtained assuming a spherical shape ($R_{{\rm p},R} = 1.623^{+0.051}_{-0.053}$ $R_{\rm Jup}$). We found a corrected value for the planetary radius of 1.681 ± 0.063 $R_{\rm Jup}$ (radius of the sphere that would have the same volume as the Roche surface of the planet) and a corresponding revised mean density of 0.318 ± 0.035 $\rho_{\rm Jup}$. These corrected values are also included in Table 6.

4.2 Atmospheric properties of WASP-103 b

We use our data to constrain the atmospheric properties of WASP-103 b. For this purpose, we modelled the atmospheric spectra of WASP-103 b, both in thermal emission and in transmission, using an exoplanetary atmospheric modelling and retrieval method based on Madhusudhan & Seager (2009) (see also Madhusudhan et al. 2011; Madhusudhan 2012). Here, we briefly summarize the method. The model consists of a 1-D radiative transfer solver which computes the observed spectrum of an exoplanetary atmosphere for a given geometry, in transit or at secondary eclipse, assuming plane parallel geometry. The temperature profile and chemical composition of the atmosphere are free parameters of the model, with six parameters for the $P - T$ profile and 4–6 free parameters for the chemical species; one parameter for each relevant atom/molecule. We include the major opacity sources expected in hot hydrogen-dominated atmospheres, namely H_2O, CO, CH_4, CO_2, C_2H_2, HCN, TiO, VO, and collision-induced absorption (CIA) due to $H_2 - H_2$, as described in Madhusudhan (2012). The model assumes hydrostatic equilibrium and local thermodynamic equilibrium (LTE) and while computing thermal emission spectra ensures global energy balance with the incident radiation. The parametric temperature structure and molecular abundances in the model allow exploration of a wide range of temperature profiles and chemical compositions in search of the best-fitting models to fit the data.

Table 6. System parameters: median values and 1σ limits of the posterior probability distribution functions derived from our global MCMC analysis.

Parameters	Values	Units
Stellar parameters		
Effective temperature $T_{\rm eff}$	6110 ± 160	K
Metallicity [Fe/H]	0.06 ± 0.13	dex
Surface gravity log $g_\star$	$4.219^{+0.013}_{-0.014}$	cgs
Mean density $\rho_\star$	$0.427^{+0.004}_{-0.006}$	$\rho_\odot$
Mass $M_\star$	1.21 ± 0.11	$M_\odot$
Radius $R_\star$	1.416 ± 0.043	$R_\odot$
Planet parameters		
Transit depth (in the R band) $dF_R = (R_{p,R}/R_\star)^2$	$1.323^{+0.046}_{-0.031}$	per cent
Transit impact parameter $b' = a\cos i_p/R_\star$	$0.06^{+0.06}_{-0.05}$	$R_\star$
Transit width W	0.1090 ± 0.0003	d
Time of inferior conjunction T_0	$2\,456\,836.296427 \pm 0.000063$	BJD_{TDB}
Orbital period P	$0.92554517 \pm 0.00000058$	d
RV semi-amplitude K	270 ± 14	$m\,s^{-1}$
Scaled semi-major axis $a/R_\star$	$3.010^{+0.008}_{-0.013}$	–
Orbital semi-major axis a	$0.01979^{+0.00057}_{-0.00061}$	AU
Orbital inclination i_p	$88.8^{+0.8}_{-1.1}$	deg
Equilibrium temperature[a] $T_{\rm eq}$	2484 ± 67	K
Surface gravity log g_p	$3.171^{+0.027}_{-0.024}$	cgs
Mean density ρ_p	$0.353^{+0.028}_{-0.024}$	$\rho_{\rm Jup}$
Mass M_p	1.51 ± 0.11	$M_{\rm Jup}$
Radius (in the R band) $R_{p,R}$	$1.623^{+0.051}_{-0.053}$	$R_{\rm Jup}$
Roche limit[b] a_R	$0.01760^{+0.00079}_{-0.00082}$	AU
a/a_R	$1.124^{+0.029}_{-0.026}$	
Planet parameters corrected for asphericity (Section 4.1)		
Radius (in the R band) $R_{p,R}$	1.681 ± 0.063	$R_{\rm Jup}$
Mean density ρ_p	0.318 ± 0.035	$\rho_{\rm Jup}$
Planet/star radius ratio $R_p/R_\star$ *(transmission spectrum)*		
$R_{p,g'}/R_\star$ (0.48 μm)	$0.1180^{+0.0018}_{-0.0016}$	–
$R_{p,r'}/R_\star$ (0.62 μm)	$0.1155^{+0.0016}_{-0.0018}$	–
$R_{p,R}/R_\star$ (0.66 μm)	$0.1150^{+0.0020}_{-0.0014}$	–
$R_{p,BB}/R_\star$ (0.70 μm)[c]	$0.1109^{+0.0024}_{-0.0018}$	–
$R_{p,i'}/R_\star$ (0.76 μm)	$0.1116^{+0.0023}_{-0.0019}$	–
$R_{p,I}/R_\star$ (0.82 μm)	0.1133 ± 0.0013	–
$R_{p,z'}/R_\star$ (0.90 μm)	$0.1143^{+0.0013}_{-0.0012}$	–
Occultation depths dF_{occ} *(emission spectrum)*		
$dF_{occ,z'}$ (0.90 μm)	699 ± 110	ppm
dF_{occ,K_S} (2.15 μm)	3567^{+400}_{-350}	ppm

Notes. [a]Assuming a null Bond albedo.
[b]Using $a_R = 2.46\,R_p(M_\star/M_p)^{1/3}$ (Chandrasekhar 1987).
[c]TRAPPIST blue-blocking filter.

4.2.1 Emission spectrum

We clearly detect the thermal emission from the dayside of the planet in both the z' (0.9 μm) and K_S (2.1 μm) bands, the measured occultation depths being 699 ± 110 ppm (6.4σ detection) and 3567^{+400}_{-350} ppm (10.2σ detection), respectively. These two measurements suggest a peculiar feature. The occultation depth in the K_S band corresponds to a brightness temperature (T_B) of 3171^{+144}_{-130} K, which is marginally higher ($\sim$1.7-σ) than the T_B obtained in the z' band of 2914^{+80}_{-87} K. Generally, for hot Jupiters, the T_B in the z' band is found to be consistent with or higher than that in the K_S band (see e.g. Anderson et al. 2013 and Lendl et al. 2013 for WASP-19 b, Madhusudhan 2012 for WASP-12 b, or Haynes et al. 2015 for WASP-33 b). This is because the z' band contains strong spectral features due to TiO. On the other hand, the K_S band is relatively devoid of strong spectral features due to TiO and other molecules relevant for hot Jupiters, with the exception of some weak features due to CO. Thus, when TiO is absent all the near-infrared ground-based photometric bands (z', J, H, and K_S) provide windows in

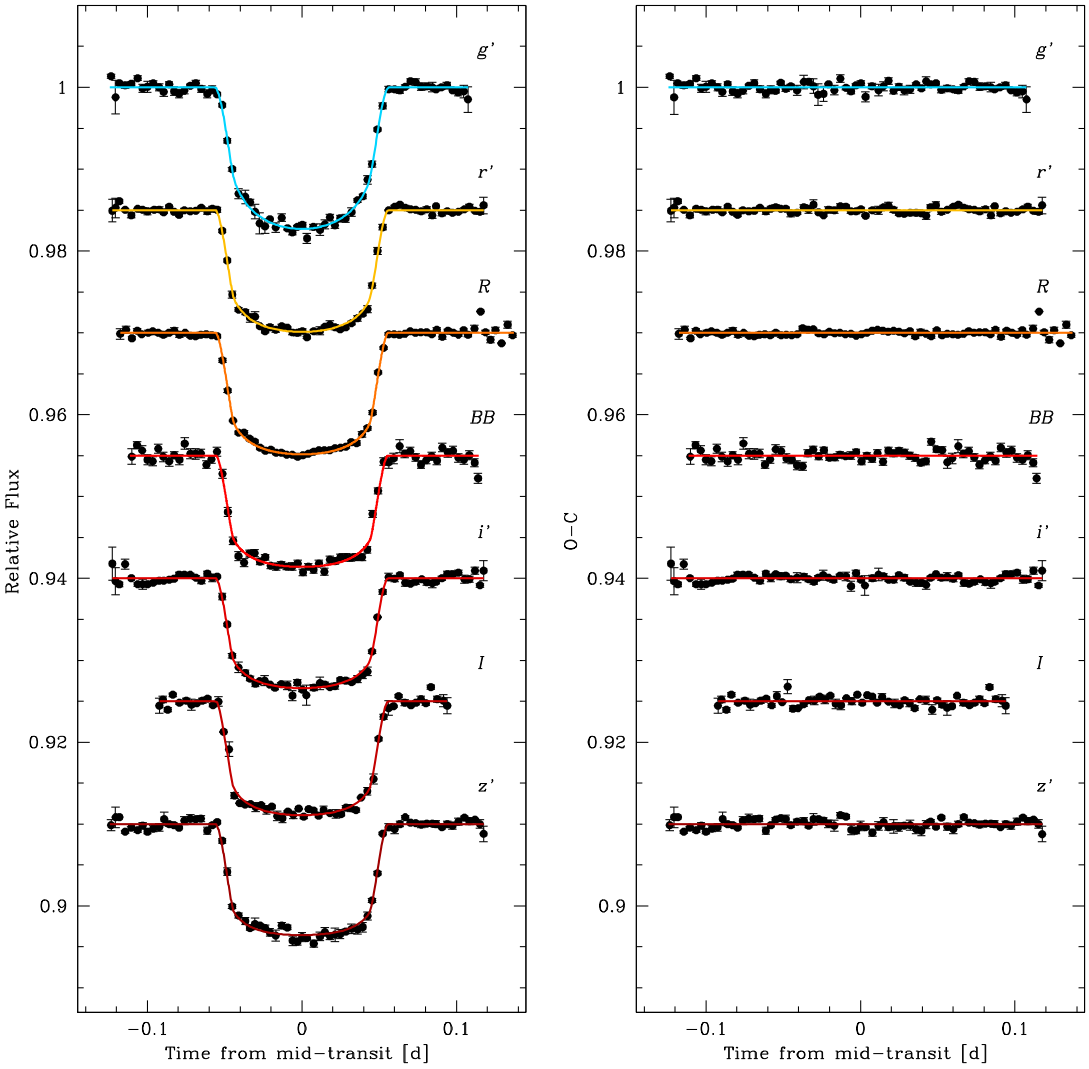

Figure 4. Left: combined transit light curves in each of the observed passbands. The data are period-folded on the best-fitting transit ephemeris from our global MCMC analysis (see Section 3.2), corrected for the photometric baseline, and binned in 5 min bins (for visual convenience). For each band, the overplotted, solid line is our best-fitting transit model. The data and models are not corrected for the dilution by the nearby star here. The light curves are shifted along the *y*-axis for clarity. Right: corresponding residuals. The RMS of the residuals in the interval [−0.09, 0.09] days are (from top to bottom) 477, 354, 249, 655, 392, 582 and 496 ppm (5 min bins).

atmospheric opacity and probe the temperatures in the deep atmosphere which tends to be isothermal for hot Jupiters. Therefore, the brightness temperatures in all these channels are expected to be similar, as observed for several hot Jupiters (e.g. Anderson et al. 2013; Lendl et al. 2013; Madhusudhan 2012). On the other hand, in hot Jupiters where TiO is present, it can lead to a thermal inversion in the atmosphere (e.g. Fortney et al. 2008) and cause spectral features in emission. In this case, the TiO features in the z' band lead to a higher T_B in that band compared to that in the K_S band which still has limited opacity (e.g. Haynes et al. 2015). Therefore, it is rarely the case that the T_B in the z' band is lower than that in the K_S band, assuming a solar composition atmosphere.

Fig. 5 shows our occultation measurements along with model emission spectra of WASP-103 b. The HST/WFC3 measurements recently reported by C17 are also shown. We consider three model scenarios in order to explain the data. First, we find that the z' band and WFC3 data are very well explained by a featureless blackbody spectrum, with a temperature of ∼2900 K (grey model in Fig. 5). A blackbody spectrum is possible if either the atmosphere is isothermal, as shown here, or the metallicity is very low, i.e. providing very low molecular opacity, irrespective of the temperature profile. However, the K_S-band point is inconsistent with this blackbody model at $\sim 3\sigma$. Secondly, a model with a thermal inversion (green model in Fig. 5) can fit the current data at nearly the same level as the blackbody. Here, the inversion model has a solar composition atmosphere, but with 0.1×solar TiO, and an inverted $P - T$ profile is shown in the inset of Fig. 5. The inversion model is able to achieve such a fit because the continuum of this model is at the same temperature as the blackbody model, with only a few strong emission features in the 1.4 μm H_2O band due to a moderately steep $P - T$ profile. Thirdly, a 0.5×solar non-inverted model (red model in Fig. 5) provides a slightly worse fit to the data. The non-inverted model has a higher continuum than the blackbody and strong H_2O absorption, neither of which is observed in the WFC3 spectrum. In summary, an isothermal temperature profile and/or a low H_2O abundance atmosphere provide the best fits to the z' band and WFC3 data. A low H_2O abundance is achievable with either a low metallicity or a high C/O ratio (Madhusudhan 2012;

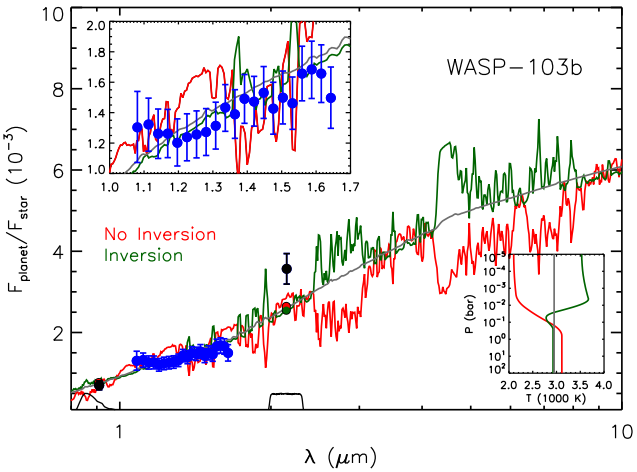

Figure 5. Observations and model spectra of dayside thermal emission from WASP-103 b. The black circles with error bars show our z'- and K_S-band measurements, while the HST/WFC3 data reported by C17 are plotted in blue. A zoom on the HST/WFC3 measurements is shown in the top inset. The colored curves show best-fitting model spectra corresponding to three model scenarios: a blackbody model with a temperature of 2900 K (grey), a model with a thermal inversion and a solar composition but a low TiO abundance (green), and a 0.5×solar model without a thermal inversion (red). The bottom inset shows the corresponding pressure-temperature profiles for the models. The green and red circles give the band-integrated fluxes of the corresponding models in the observed photometric bands (bottom black curves), for comparison to the data.

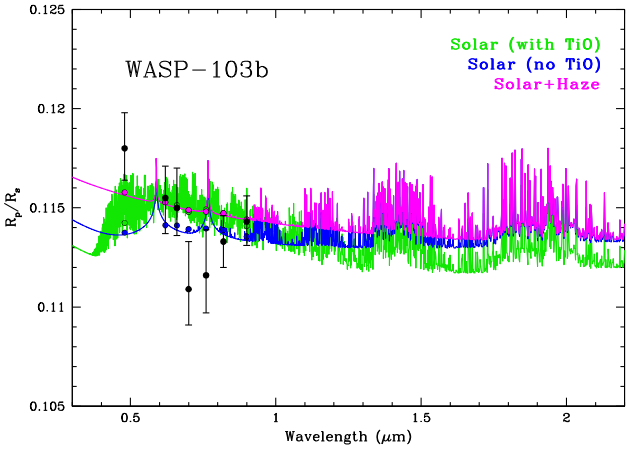

Figure 6. Broad-band measurements of the planet-to-star radius ratio ($R_p/R_\star$) as a function of wavelength compared to model transmission spectra of WASP-103 b. The various measurements are shown as black circles with error bars. The colored curves show three different plausible models: a fiducial model with solar abundance composition in thermochemical equilibrium (TE) without TiO (blue), a solar abundance model in TE with TiO (green) and a solar abundance model with enhanced scattering due to a possible haze with a scattering index of −3.5 (magenta). The colored circles give the band-integrated fluxes of the corresponding models in the observed photometric bands, for comparison to the data.

Moses et al. 2013). Our model inferences are consistent with those of C17, who based their results on the WFC3 data alone.

On the other hand, as can be seen in Fig. 5, our K_S-band data point is matched only at 2σ–3σ by our current models. To reproduce this high K_S-band flux, a strong source of opacity in this wavelength band would be needed. Such a scenario would also require a strong thermal inversion, as well as low H_2O and TiO abundances. A thermal inversion would be needed to produce a K_S-band emission feature from the above opacity source over the continuum blackbody which is required in the WFC3 band. And, the low H_2O and TiO abundances would be required to satisfy the lack of features in the WFC3 and z' bands, respectively. However, as pointed out previously, the K_S band is not expected to contain strong spectral features due to any of the molecules relevant for a hot-Jupiter atmosphere, making the above scenario rather unlikely. Further observations in the K_S band are thus required to confirm our measurement, which is based on a single occultation light curve, before any adequate interpretation of the data can be given.

Additional data are necessary to better characterize the dayside atmosphere of WASP-103 b. Most notably, observations with *Spitzer* can distinguish between our three model scenarios. The *Spitzer*/IRAC photometric bands at 3.6 and 4.5 μm together should be able to provide strong constraints on the CO absorption versus emission features between the non-inverted and inverted models in the 4–5 micron region. The joint constraints on the CO and H_2O abundances could then help constrain the C/O ratio of the dayside atmosphere (Madhusudhan 2012). As mentioned above, we also encourage further observations in the K_S band to confirm our high emission measurement in that band. On a longer time frame, the *James Webb Space Telescope* (JWST) should be able to provide conclusive constraints on the $P-T$ profile and composition of this planetary atmosphere.

4.2.2 *Transmission spectrum*

The planet-to-star radius ratios ($R_p/R_\star$) obtained for each of the observed passbands are given in Table 6 and shown in Fig. 6. We find the same 'V-shape' pattern as S16, with a minimum effective planetary radius around 700 nm and increasing values towards both shorter and longer wavelengths. This pattern is however less significant in our transmission spectrum, due to our more conservative error bars (cf. Section 3.1).

We compared our broad-band measurements to different model transmission spectra of WASP-103 b, with the aim to derive constraints on the atmospheric properties of the planet at the day–night terminator region. The possible sources of opacity in the spectral range covered (0.4−1.0 μm) for a typical hot Jupiter in the temperature regime of WASP-103 b, with an equilibrium temperature of ∼2500 K are: (*a*) H_2O at the redder wavelengths, (*b*) TiO and VO over the entire range, (*c*) Na and K doublet line opacity peaking at 0.59 μm and 0.78 μm, respectively, (*d*) Rayleigh scattering due to H_2, and (*e*) potential high-temperature refractory hazes, e.g. of Fe particles. Amongst all these sources of opacity, the most prominent sources are TiO and scattering. Given the broad-band photometric nature of the data, we are unable to resolve any particular spectral features. However, first, the prominent sources of opacity, e.g. TiO, are significantly broad to influence the data. Secondly, the full visible coverage of the data allows us to investigate a possible blueward slope in the data, which, in turn, could constrain the sources of scattering in the atmosphere, including the presence of hazes.

We explored the model parameter space of the opacity sources discussed above in search of models that can explain the data. Fig. 6 shows three models with different degrees of fit:

(i) a fiducial model with solar abundance composition in thermochemical equilibrium (TE), but with no TiO (blue);
(ii) a solar abundance model in TE with TiO (green);

Table 7. χ^2 values calculated from the data and the various models of the transmission spectrum of WASP-103 b, considering all data (second column) and omitting the g'-band measurement (third column).

Model	All data	Without the g'-band measurement
Solar without TiO	9.6	4.0
Solar with TiO	10.3	6.0
Solar with haze	7.5	5.9

(iii) a solar abundance model with enhanced scattering due to a possible haze with a scattering index of −3.5, instead of −4 for H_2 Rayleigh scattering (magenta).

The corresponding χ^2 values are given in Table 7. When considering the entire data set, we find that the model with haze provides a better fit to the data than the two other models. However, we note cautiously that this result relies heavily on the high $R_p/R_\star$ measured in the bluest wavelength band in our data, i.e. the g' band. When this data point is not considered, the best fit is obtained by the fiducial solar-composition model without TiO (Table 7, last column). It is clear however that none of these models match the data well.

During the refereeing process of this paper, a higher resolution optical transmission spectrum of WASP-103 b obtained with Gemini/GMOS was published by Lendl et al. (2017). These data, covering the wavelength range between 550 and 960 nm, do not show any signs of the V-shape pattern found in our measurements. Instead, they show increased absorption in the cores of the Na and K line features, without any other evident trend, thus pointing to a rather clear atmosphere for WASP-103 b at the pressure levels probed (between 0.01 and 0.1 bar). We have no satisfactory explanation for this discrepancy at this point. Our transmission spectrum is mostly based on the data set published by S15 and re-analysed by S16 (17 out of the 25 transit light curves we used). Our independent data analysis gives similar results to theirs, suggesting that the unusual profile of the measured transmission spectrum is intrinsic to the data and is not related to the data analysis process.

Extending WASP-103 b's measured transmission spectrum towards near-infrared wavelengths, for example with HST/WFC3, would allow a more detailed characterization of its atmosphere at the day–night terminator region by constraining its H_2O abundance. Additional data at shorter wavelengths than the spectral range covered by the GMOS data (i.e. bluewards of 550 nm) would also be useful to definitely assess the presence of a scattering slope possibly related to hazes in WASP-103 b's transmission spectrum. In this context, it is worth mentioning that a near-UV transit light curve of WASP-103 b has been published very recently (after our paper was accepted) by Turner et al. (2017), who report a ($R_p/R_\star$) value of 0.1181 ± 0.0016 in the Bessel U filter (303-417 nm), in excellent agreement with our g'-band measurement. At the high temperature ($\gtrsim$2000 K) of WASP-103 b, most of the usual condensate species are in gas phase (see e.g. Marley et al. 2013), with the exception of few such as Fe and Al_2O_3. Characterizing the presence of hazes in such atmospheres is important to be able to make robust determinations of chemical abundances from future spectroscopic data using HST and JWST.

5 CONCLUSIONS

In this work, we presented a total of 19 new eclipse light curves for the ultra-short-period hot Jupiter WASP-103 b. Sixteen of these light curves were obtained during occultations and three during transits. We also obtained five new RV measurements. We combined these new observations with previously published data and performed a global MCMC analysis of the resulting extensive data set (41 eclipse light curves and 23 RVs), taking into account the contamination from a faint nearby star.

Using the approach presented in Lendl et al. (2013), which involves combining a large number (here 15) of occultation light curves obtained with ∼1 m-class telescopes to mitigate the effects of correlated noise and progressively extract the occultation signal from the noise, we detected the dayside emission of the planet in the z' band at better than 6σ (699±110 ppm). From a single occultation light curve acquired with the CFHT/WIRCam facility, we also detected the planet's dayside emission in the K_S band at better than 10σ, the measured occultation depth being 3567^{+400}_{-350} ppm. We compared these two measurements, along with recently published HST/WFC3 spectrophotometric data, to model emission spectra of WASP-103 b with different temperature profiles and chemical compositions. On one hand, we found that the z' band and WFC3 data are best fit by an isothermal atmosphere at a temperature of ∼2900 K, or an atmosphere with a low metallicity or a high C/O ratio. On the other hand, we found an unexpectedly high flux in the K_S band when compared to these atmospheric models, which requires confirmation with additional observations before any interpretation can be given.

From our global data analysis, we also derived a broad-band optical transmission spectrum that shows a minimum around 700 nm and increasing values towards both shorter and longer wavelengths. This is in agreement with the results of the study by S16, which was based on a large fraction of the archival transit light curves included in our analysis. The unusual profile of this transmission spectrum is poorly matched by theoretical spectra and is not confirmed by more recent observations at higher spectral resolution reported by Lendl et al. (2017).

Future observations with existing (HST, *Spitzer*) or planned (JWST) facilities, both in emission and transmission, should be able to provide better constraints on the $P - T$ profile and chemical composition of WASP-103 b's atmosphere. In particular, we encourage further observations in the K_S band to confirm our high emission measurement in that band. Improving our understanding of this planetary system also requires a more precise characterization of the faint nearby star, by obtaining additional adaptive-optics observations with a large-aperture telescope.

ACKNOWLEDGEMENTS

The research leading to these results has received funding from the European Community's Seventh Framework Programme (FP7/2013-2016) under grant agreement number 312430 (OPTICON). The Canada-France-Hawaii Telescope (CFHT) is operated by the National Research Council of Canada, the Institut National des Sciences de l'Univers of the Centre National de la Recherche Scientifique of France, and the University of Hawaii. The authors thank the CFHT staff, especially Pascal Fouqué, for scheduling, helping prepare, and conducting the CFHT/WIRCam observations used in this work. TRAPPIST is a project funded by the Belgian Fund for Scientific Research (Fonds National de la Recherche Scientifique, F.R.S.-FNRS) under grant FRFC 2.5.594.09.F, with the participation of the Swiss National Science Fundation (SNF). The Swiss *Euler* Telescope is operated by the University of Geneva, and is funded by the Swiss National Science Foundation. L. Delrez acknowledges support from the Gruber Foundation Fellowship.

M. Gillon and E. Jehin are F.R.S.-FNRS Research Associates. The authors thank the anonymous reviewers for their valuable suggestions.

REFERENCES

Anderson D. R. et al., 2013, MNRAS, 430, 3422
Baranne A. et al., 1996, A&AS, 119, 373
Budaj J., 2011, AJ, 141, 59
Burrows A. S., 2014, Nature, 513, 345
Cartier K. M. S. et al., 2017, AJ, 153, 34 (C17)
Chandrasekhar S., 1987, Ellipsoidal Figures of Equilibrium. Dover, New York
Charbonneau D., Brown T. M., Noyes R. W., Gilliland R. L., 2002, ApJ, 568, 377
Charbonneau D. et al., 2005, ApJ, 626, 523
Claret A., Bloemen S., 2011, A&A, 529, A75
Collier Cameron A. et al., 2007, MNRAS, 380, 1230
Croll B. et al., 2015, ApJ, 802, 28
Delrez L. et al., 2016, MNRAS, 458, 4025
Deming D., Seager S., 2009, Nature, 462, 301
Deming D., Seager S., Richardson L. J., Harrington J., 2005, Nature, 434, 740
Deming D. et al., 2013, ApJ, 774, 95
Devost D., Albert L., Teeple D., Croll B., 2010, Proc. SPIE, 7737, 77372D
Diamond-Lowe H., Stevenson K. B., Bean J. L., Line M. R., Fortney J. J., 2014, ApJ, 796, 66
Eastman J., Siverd R., Gaudi B. S., 2010, PASP, 122, 935
Enoch B., Collier Cameron A., Parley N. R., Hebb L., 2010, A&A, 516, A33
Evans T. M. et al., 2017, Nature, 548, 58
Fortney J. J., Lodders K., Marley M. S., Freedman R. S., 2008, ApJ, 678, 1419
Fu G., Deming D., Knutson H., Madhusudhan N., Mandell A., Fraine J., 2017, ApJ, 847, L22
Gelman A., Rubin D., 1992, Stat. Sci., 7, 457
Gibson N. P., Aigrain S., Barstow J. K., Evans T. M., Fletcher L. N., Irwin P. G. J., 2013, MNRAS, 428, 3680
Gillon M., Jehin E., Magain P., Chantry V., Hutsemékers D., Manfroid J., Queloz D., Udry S., 2011, in Bouchy F., Díaz R., Moutou C., eds, EPJ Web of Conf., Vol. 11, Detection and Dynamics of Transiting Exoplanets. EDP Sciences, France, p. 06002
Gillon M. et al., 2011b, A&A, 533, A88
Gillon M. et al., 2012, A&A, 542, A4
Gillon M. et al., 2014, A&A, 562, L3(G14)
Hansen C. J., Schwartz J. C., Cowan N. B., 2014, MNRAS, 444, 3632
Haynes K., Mandell A. M., Madhusudhan N., Deming D., Knutson H., 2015, ApJ, 806, 146
Hellier C. et al., 2011, Eur. Phys. J. Web Conf., 11, 01004
Hubeny I., Burrows A., Sudarsky D., 2003, ApJ, 594, 1011
Husser T.-O., Wende-von Berg S., Dreizler S., Homeier D., Reiners A., Barman T., Hauschildt P. H., 2013, A&A, 553, A6
Jehin E. et al., 2011, Messenger, 145, 2
Knutson H. A., Charbonneau D., Allen L. E., Burrows A., Megeath S. T., 2008, ApJ, 673, 526
Knutson H. A., Charbonneau D., Burrows A., O'Donovan F. T., Mandushev G., 2009, ApJ, 691, 866
Knutson H. A., Howard A. W., Isaacson H., 2010, ApJ, 720, 1569
Lendl M. et al., 2012, A&A, 544, A72
Lendl M., Gillon M., Queloz D., Alonso R., Fumel A., Jehin E., Naef D., 2013, A&A, 552, A2
Lendl M. et al., 2016, A&A, 587, A67
Lendl M., Cubillos P. E., Hagelberg J., Müller A., Juvan I., Fossati L., 2017, A&A, 606, A18
Line M. R., Knutson H., Deming D., Wilkins A., Desert J.-M., 2013, ApJ, 778, 183
Machalek P., McCullough P. R., Burke C. J., Valenti J. A., Burrows A., Hora J. L., 2008, ApJ, 684, 1427
Madhusudhan N., 2012, ApJ, 758, 36
Madhusudhan N., Seager S., 2009, ApJ, 707, 24
Madhusudhan N., Mousis O., Johnson T. V., Lunine J. I., 2011, ApJ, 743, 191
Madhusudhan N., Knutson H., Fortney J. J., Barman T., 2014, in Beuther H., Klessen R. S., Dullemond C. P., Henning T., eds, Protostars and Planets VI. Univ. Arizona Press, Tucson, p. 739
Madhusudhan N., Agúndez M., Moses J. I., Hu Y., 2016, Space Sci. Rev., 205, 285
Mandel K., Agol E., 2002, ApJ, 580, L171
Marley M. S., Ackerman A. S., Cuzzi J. N., Kitzmann D., 2013, Clouds and Hazes in Exoplanet AtmospheresUniv. Arizona Press, Tucson, p. 367
Moses J. I., Madhusudhan N., Visscher C., Freedman R. S., 2013, ApJ, 763, 25
Murray C. D., Correia A. C. M., 2010, Keplerian Orbits and Dynamics of Exoplanets. p. 15
Ngo H. et al., 2016, ApJ, 827, 8 (N16)
Nikolov N. et al., 2014, MNRAS, 437, 46
Nikolov N. et al., 2015, MNRAS, 447, 463
Nugroho S. K., Kawahara H., Masuda K., Hirano T., Kotani T., Tajitsu A., 2017, AJ, 154, 221
Pepe F., Mayor M., Galland F., Naef D., Queloz D., Santos N. C., Udry S., Burnet M., 2002, A&A, 388, 632
Pollacco D. L. et al., 2006, PASP, 118, 1407
Press W. H., Teukolsky S. A., Vetterling W. T., Flannery B. P., 1992, Numerical Recipes in FORTRAN. The Art of Scientific Computing. Cambridge Univ. Press, Cambridge, UK
Puget P. et al., 2004, in Moorwood A. F. M., Iye M., eds, Proc. SPIE Conf. Ser. Vol. 5492, Ground-based Instrumentation for Astronomy. SPIE, Bellingham, p. 978
Queloz D. et al., 2000, A&A, 354, 99
Queloz D. et al., 2001, A&A, 379, 279
Schwarz G. E., 1978, Ann. Statist., 6, 461
Schwarz H., Brogi M., de Kok R., Birkby J., Snellen I., 2015, A&A, 576, A111
Seager S., Mallén-Ornelas G., 2003, Astrophys. J., 585, 1038
Seager S., Sasselov D. D., 2000, ApJ, 537, 916
Sing D. K. et al., 2011, A&A, 527, A73
Sing D. K. et al., 2013, MNRAS, 436, 2956
Sing D. K. et al., 2015, MNRAS, 446, 2428
Sing D. K. et al., 2016, Nature, 529, 59
Skrutskie M. F. et al., 2006, AJ, 131, 1163
Southworth J., 2011, MNRAS, 417, 2166
Southworth J., Evans D. F., 2016, MNRAS, in press (S16)
Southworth J. et al., 2015, MNRAS, 447, 711(S15)
Spiegel D. S., Silverio K., Burrows A., 2009, ApJ, 699, 1487
Stetson P. B., 1987, PASP, 99, 191
Straižys V., Lazauskaitė R., 2009, Baltic Astron., 18, 19
Tsiaras A. et al., 2017, ApJ, preprint (arXiv:1704.05413)
Turner J. D. et al., 2017, MNRAS, 472, 3871
Vacca W. D., Cushing M. C., Rayner J. T., 2004, PASP, 116, 352
Wang W., van Boekel R., Madhusudhan N., Chen G., Zhao G., Henning T., 2013, ApJ, 770, 70
Winn J. N., 2010, Transits and Occultations, Exoplanets. Univ. Arizona Press, Tucson, p. 55
Wöllert M., Brandner W., 2015, A&A, 579, A129(W15)
Zhou G., Bayliss D. D. R., Kedziora-Chudczer L., Salter G., Tinney C. G., Bailey J., 2014, MNRAS, 445, 2746

APPENDIX A: INDIVIDUAL ECLIPSE LIGHT CURVES

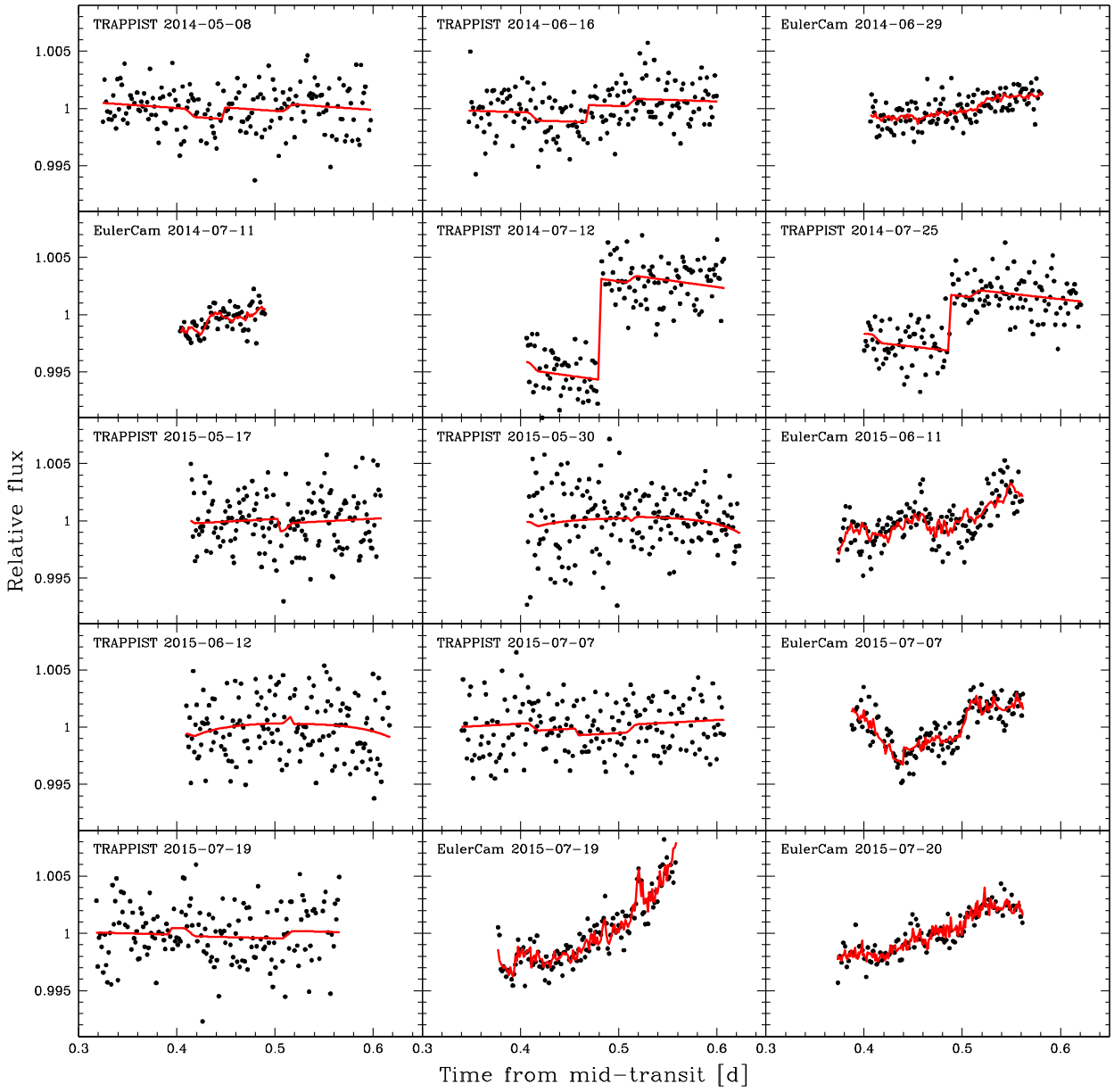

Figure A1. All raw occultation light curves obtained in the z' band with TRAPPIST and Euler/EulerCam. The data are period-folded on the best-fitting transit ephemeris from our global MCMC analysis (see Section 3.2) and binned in 2 min bins. For each light curve, the best-fitting full model (photometric baseline × occultation in the z' band) is overplotted in red. The data and models are not corrected for the dilution by the nearby star here.

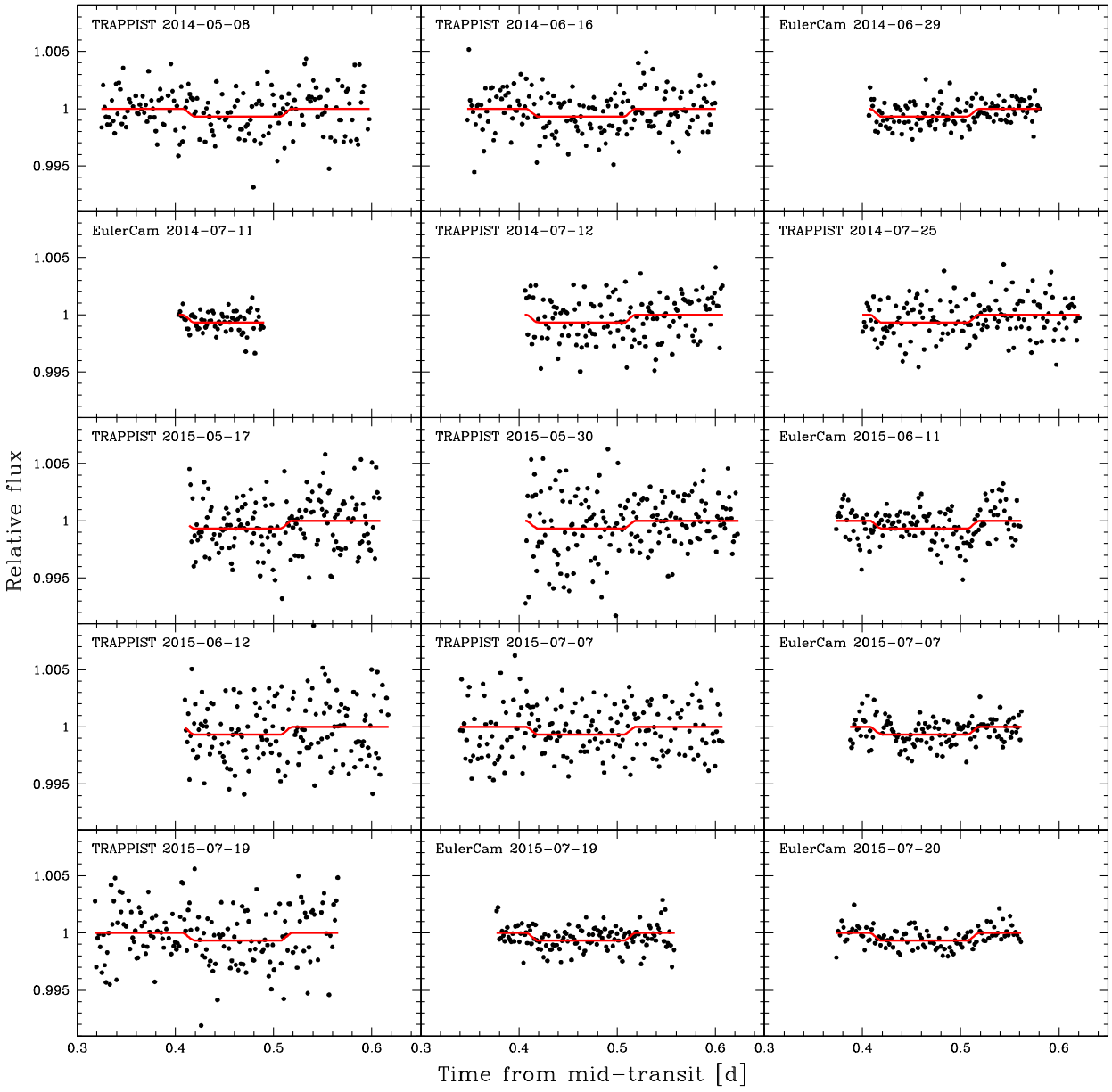

Figure A2. Same light curves as in Fig. A1, but divided by their best-fitting baseline models (different for each light curve). The best-fitting occultation model in the z' band is overplotted in red. The data and model are not corrected for the dilution by the nearby star here.

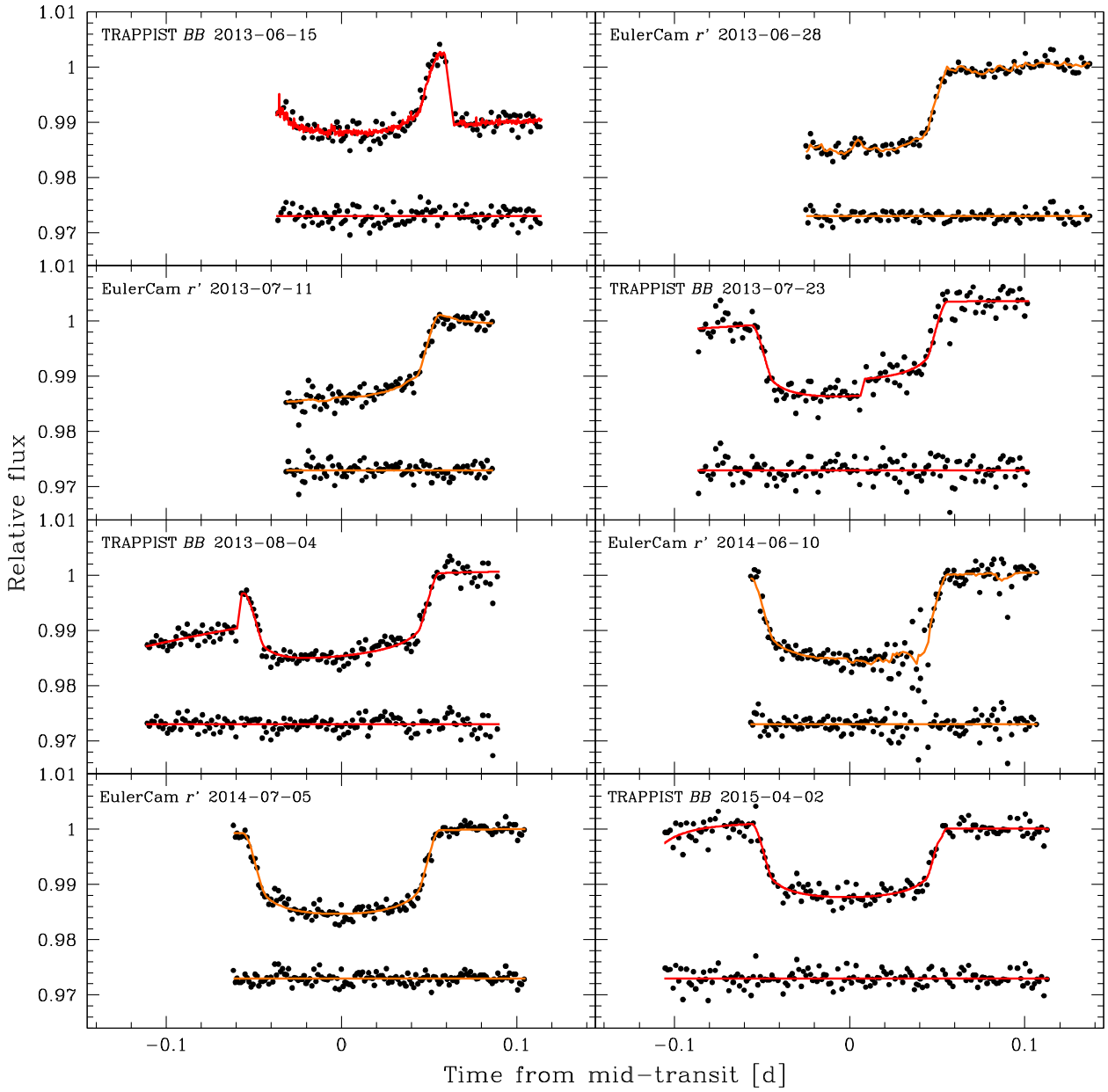

Figure A3. All raw TRAPPIST and Euler/EulerCam transit light curves used in this work. The data are period-folded on the best-fitting transit ephemeris from our global MCMC analysis (see Section 3.2) and binned in 2 min bins. For each light curve, the overplotted solid line is the best-fitting full model (photometric baseline × transit). The data and models are not corrected for the dilution by the nearby star here. The first five light curves were published in G14, while the last three ones are new data.

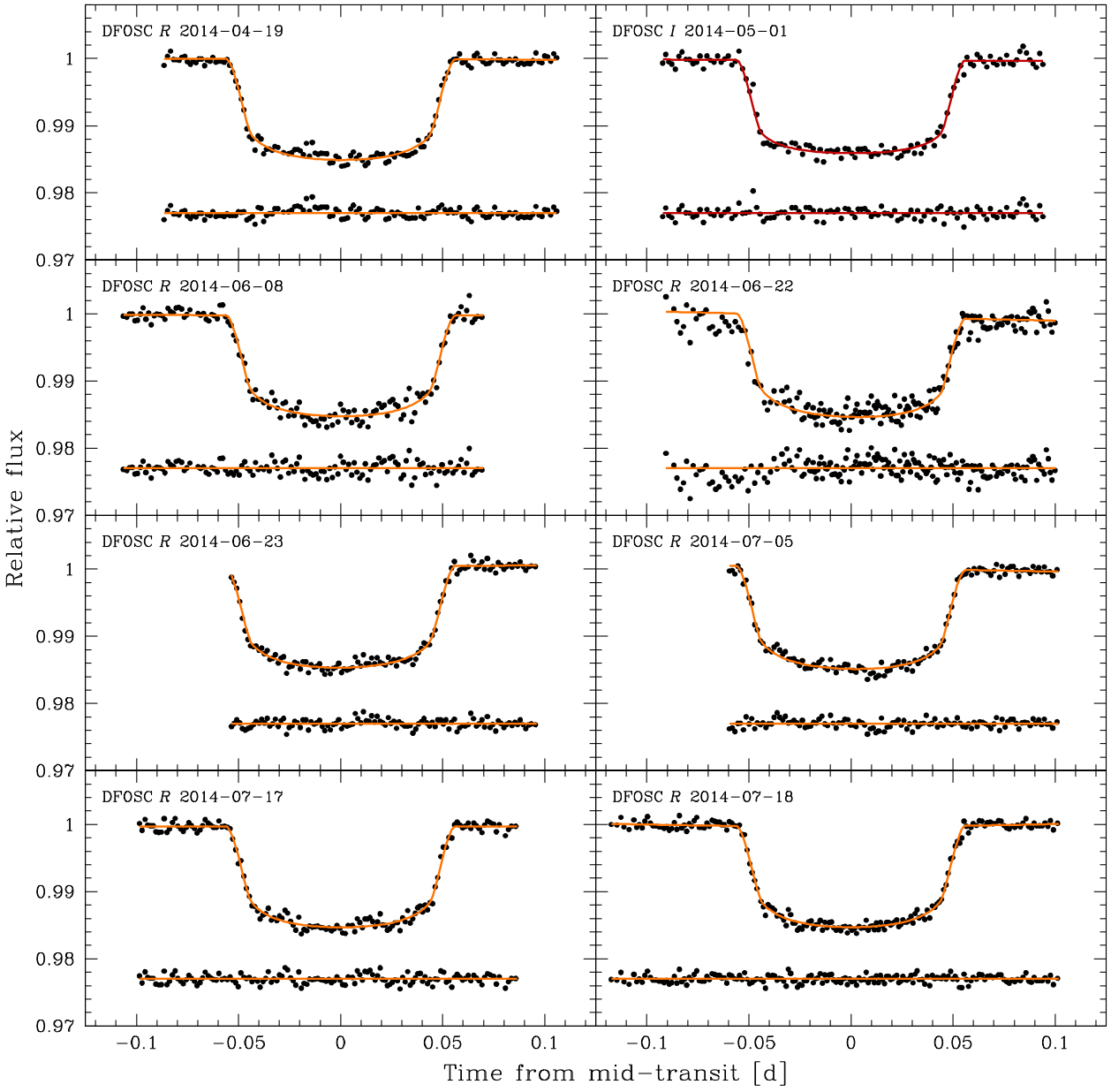

Figure A4. All raw Danish/DFOSC transit light curves used in this work. The data are period-folded on the best-fitting transit ephemeris from our global MCMC analysis (see Section 3.2) and binned in 2 min bins. For each light curve, the overplotted solid line is the best-fitting full model (photometric baseline × transit). The data and models are not corrected for the dilution by the nearby star here. All these light curves were published in S15.

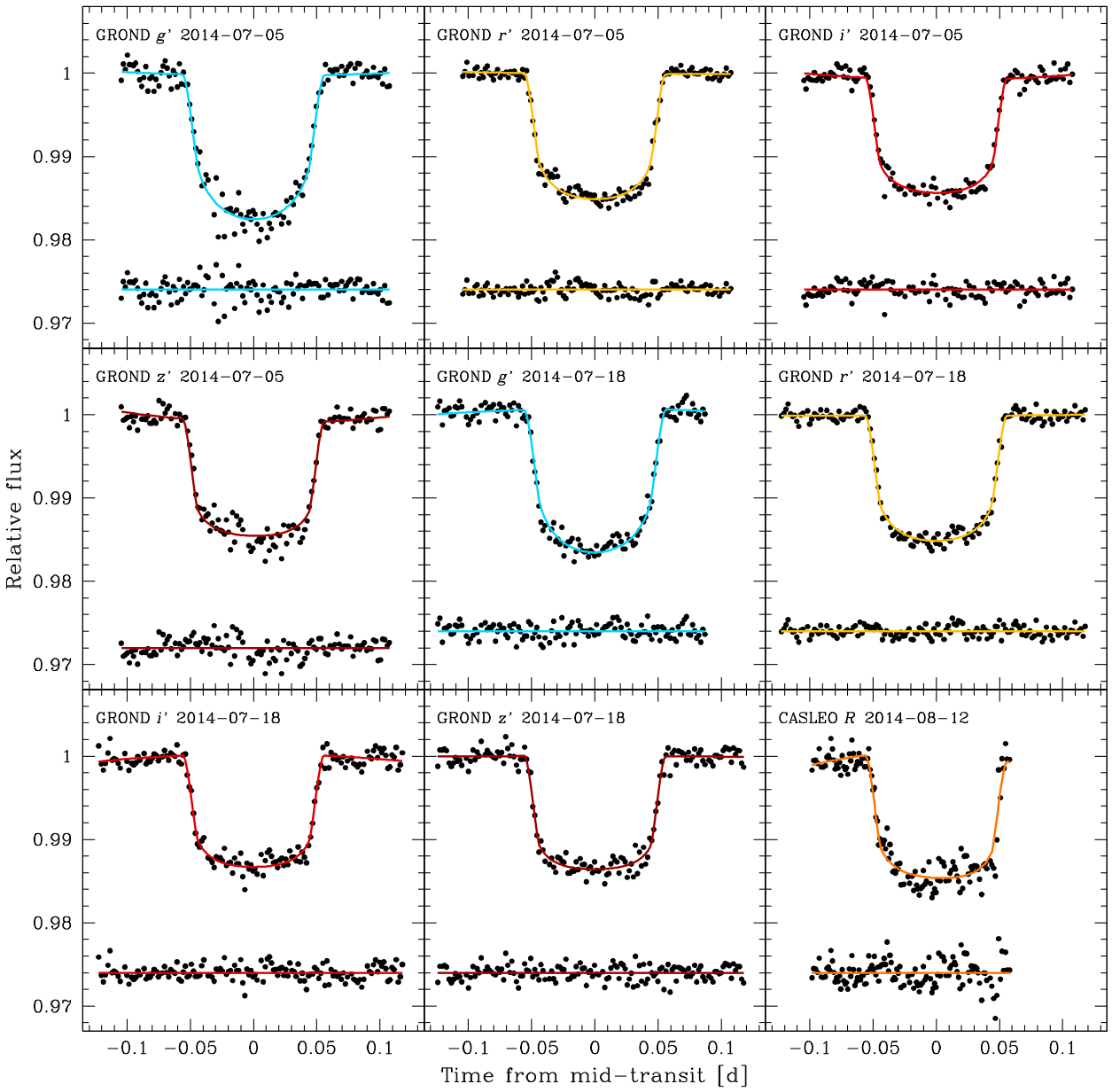

Figure A5. All raw 2.2 m/GROND and CASLEO/2.15 m transit light curves used in this work. The data are period-folded on the best-fitting transit ephemeris from our global MCMC analysis (see Section 3.2) and binned in 2 min bins. For each light curve, the overplotted solid line is the best-fitting full model (photometric baseline × transit). The data and models are not corrected for the dilution by the nearby star here. All these light curves were published in S15.

This paper has been typeset from a TEX/LATEX file prepared by the author.